Photo-carrier radiometry of semiconductors: A novel powerful optoelectronic diffusion-wave technique for silicon process non-destructive evaluation

Andreas Mandelis

Center for Advanced Diffusion-Wave Technologies, Department of Mechanical and Industrial Engineering, University of Toronto, Toronto, Ont., Canada M5S 3G8

Available online 24 October 2005

Abstract

Laser-induced infrared photo-carrier radiometry (PCR) is introduced as an emerging semiconductor NDT technology, both theoretically and experimentally through deep sub-surface scanning imaging and signal frequency dependencies from Si wafers. PCR completely obliterates the thermal infrared emission band (8–12 μm), unlike the known photothermal signal types, which invariably contain combinations of carrier-wave and thermal-wave infrared emissions due to the concurrent lattice absorption of the incident beam and non-radiative heating. The PCR theory is presented as infrared depth integrals of carrier-wave (CW) density profiles. Experimental aspects of this new methodology are given, including the determination of photo-carrier transport parameters (surface recombination velocities, carrier diffusion coefficients, recombination lifetimes and carrier mobilities) through modulation frequency scans. CW scanning imaging is also introduced. High-frequency, deep-defect PCR images thus obtained prove that very-near-surface (where optoelectronic device fabrication takes place) photo-carrier generation can be detrimentally affected not only by local electronic defects as is commonly assumed, but also by defects in remote wafer regions much deeper than the extent of the electronically active thin surface layer.
© 2005 Elsevier Ltd. All rights reserved.

1. Introduction

In recent years, the development of laser-induced infrared photothermal radiometry (PTR) of semiconductors in our laboratory as a quantitative methodology for the measurement of transport properties of semiconductors has led to several advances in the non-contact measurement of four transport parameters: bulk recombination lifetime, (two) surface recombination velocities and carrier diffusion coefficient in Si and GaAs. Reviews of the subject matter have been presented by Mandelis [1] and Christofides et al. [2]. The major advantage of PTR over other photothermal techniques, such as photomodulated thermoreflectance (PMOR), has been found to be the higher sensitivity of PTR to the photo-excited free carrier-density-wave (the modulated-laser driven oscillating electronic diffusion-wave [3]) than PMOR [4,5]. This advantage exists due to domination of the free-carrier wave over the superposed thermal-wave (TW) contributions to the PTR signal. Even

so, the ever-present thermal-wave contributions due to direct lattice absorption, followed by non-radiative energy conversion and blackbody (thermal infrared) emissions, have resulted in PTR signal interpretational and computational difficulties due to the large number of variables involved [6]. Therefore, confidence in the measured values of the four electronic transport properties is always accompanied by the hurdle of assuring uniqueness of the measured set of parameters in any given situation. Given the fundamental and practical importance of developing an all-optical, non-destructive and non-intrusive diagnostic methodology for monitoring the transport properties of semiconductors, and in view of the inability of photothermal semiconductor diagnostic methods [2,7] to eliminate the thermal-wave contributions, we concluded that the search for a purely carrier-wave laser-based detection technique must move in the direction of isolating and filtering out the superposition of thermal-wave contributions to the infrared emission spectrum.

In a photo-excited semiconductor of bandgap energy E_G, an externally incident optical source such as a laser beam

with super-bandgap energy photons $\hbar\omega_{vis} > E_G$ will be absorbed and can generate free carriers which may subsequently follow several deexcitation pathways. Ultra-fast decay to the respective bandedge (e.g. conduction band) through non-radiative transitions and emission of phonons, will raise the temperature of the semiconductor locally. The free carriers will further diffuse within their statistical lifetime and will recombine with carriers of the opposite sign across the bandgap or into impurity and/or defect states within the bandgap. The electron-hole recombination mechanism with or without phonon assistance will lead either to non-radiative energy conversion through phonon emissions (e.g. in indirect-gap semiconductors such as Si) which will further raise the temperature, or to radiative decay which will produce photons of near- or sub-bandgap energy. In actual semiconductor materials, there may be a distribution of impurity and defect states into which de-excitation may occur. Therefore, it is more relevant to consider the full spectral range of IR emissions from a photo-excited semiconductor crystal: $\hbar\omega_{IR} = \hbar\omega(\lambda_D)$. If the exciting super-bandgap radiation is intensity-modulated at frequency $f = \omega/2\pi$, then the photo-generated free carrier density constitutes a spatially damped carrier-density wave (CW) (or carrier-diffusion wave [3]), which oscillates diffusively away from the generating source under its concentration gradient and recombines with a phase lag dependency on a delay time equal to its statistical lifetime, τ, a structure- and process-sensitive property [8].

Under conditions that apply to a number of semiconductors [9], electronic transitions in these materials occur essentially adiabatically, with minimum thermal energy exchange interactions across well-defined electronic state densities, leading to validation of Kirchhoff's Law of Detailed Balance [10] through complete thermal decoupling of the CW oscillator ensemble. A by-product of adiabaticity is that the IR spectra of thermal and carrier recombination emissions are independent of each other, a feature which is central to the realization of Photo-Carrier Radiometry (PCR).

2. Principles of photo-carrier radiometry

Fig. 1 shows an elementary slice of thickness dz centered at depth z in a semiconductor slab. The crystal is supported by a backing, but is not necessarily in contact with the backing. A modulated laser beam at angular frequency $\omega = 2\pi f$ and wavelength λ_{vis} impinges on the front surface of the semiconductor. The super-bandgap radiation is absorbed within a (short) distance from the surface, typically, a few μm, given by $[\alpha(\lambda_{vis})]^{-1}$ where $\alpha(\lambda_{vis})$ is the visible-range absorption coefficient of the pump radiation. The ensuing de-excitation processes generally involve radiative and non-radiative energy release components, resulting in the generation of an IR photon field in the semiconductor involving a relatively broad spectral bandwidth. At thermal and electronic equilibrium, assuming a one-dimensional
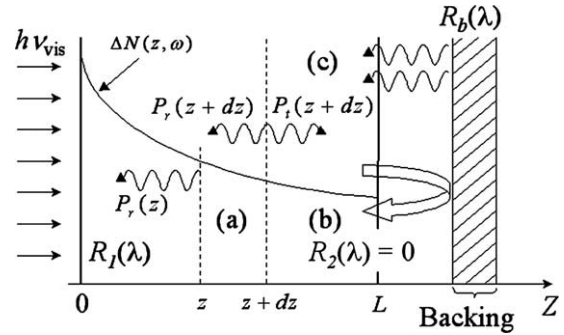
Fig. 1. Cross-sectional view of contributions to front-surface radiative emissions of IR photons from: (a) a semiconductor strip of thickness dz at depth z; (b) re-entrant photons from the back surface due to reflection from a backing support material; (c) emissive IR photons from the backing at thermodynamic temperature T_b. The carrier-wave depth profile $\Delta N(z,\omega)$ results in a depth dependent IR absorption/emission coefficient due to free-carrier absorption of the infrared photon fields, both ac and dc.

geometry as a result of a large laser beam spotsize and/or thin sample, the emitted IR photons have equal probability of being directed toward the front or the back surface of the material. A detailed account of all IR emission, absorption, and reflection processes [9] yields the expression for the total IR emissive power at the fundamental frequency across the front surface of the material in the presence of a backing support which acts both as reflector of semiconductor-generated IR radiation with spectrum centered at λ, and as emitter of backing-generated IR radiation centered at wavelength λ_b

$$P_T \approx \int_{\lambda_2}^{\lambda_1} d\lambda [1 - R_1(\lambda)] \Bigg\{ (1 + R_b(\lambda)[1 + R_1(\lambda)]) \varepsilon_o(\lambda)$$
$$\times \int_0^L \Delta W_P(z,\omega;\lambda) dz + [(1 + R_b(\lambda)[1 + R_1(\lambda)]) W_o(T_o;\lambda)$$
$$- W_P(T_b,\lambda) e(T_b,\lambda)[1 - R_1(\lambda)]] \int_0^L \varepsilon_{fc}(z,\omega;\lambda) dz \Bigg\}$$

$$(1)$$

where R_1 is the front surface reflectivity, R_b is the backing support material reflectivity, $\varepsilon_o(\lambda)$ is the background IR emission coefficient of the material, $\varepsilon_{fc}(z,\omega;\lambda)$ is the IR emission coefficient due to the free photoexcited carrier wave, $e(T_b,\lambda)$ is the spectral emissivity of the backing material, $\Delta W_P(z,\omega,\lambda) dz$ is the harmonic IR emissive power due to the harmonically varying temperature of the sample, $W_o(T_o;\lambda)$ is the unmodulated emissive spectral power per unit wavelength due to both Planck-mediated $[W_{Po}(T_o,\lambda)]$ and direct radiative $[\eta_R W_{eR}(\lambda)]$ emissions, $W_P(T_b,\lambda)$ is the spectral emissive power per unit wavelength of the backing surface at temperature T_b, and $[\lambda_1, \lambda_2]$ is the spectral bandwidth of the detector. $W_{eR}(\lambda)$ is the spectral power per unit wavelength, the product of the recombination

transition rate from band to band, or from bandedge to defect or impurity state, as the case may be, multiplied by the energy difference between initial and final states. η_R is the quantum yield for IR radiative emission upon carrier recombination into one of these states. During our experimental attempts to separate out carrier-wave and thermal-wave contributions which are always strongly mixed as in Eq. (1), we found that they can be separated out effectively only through spectral filtering and bandwidth matching at the IR detector, thus introducing the technique of photo-carrier radiometry (PCR).

Instrumental filtering of all thermal infrared emission contributions and bandwidth matching to the IR photo-detector allows for all Planck-mediated terms to be eliminated from Eq. (1) yielding:

$$
P(\omega) \approx \int_{\lambda_2}^{\lambda_1} d\lambda [1 - R_1(\lambda)](1 + R_b(\lambda)[1
$$

$$
+ R_1(\lambda)])\eta_R W_{eR}(\lambda) \int_0^L \varepsilon_{fc}(z, \omega; \lambda) dz \qquad (2)
$$

The absorption (and, equivalently, assuming Kirchhoff's Law is valid, the emission) coefficient depends on the free-carrier density as [11]

$$
\varepsilon_{fc}(z, \omega; \lambda) = \alpha_{IRfc}(z, \omega; \lambda) = \frac{q\lambda^2}{4\pi^2 \varepsilon_{oD} c^3 n m^{*2} \mu} \Delta N(z, \omega; \lambda)
$$
$$
(3)
$$

for relatively low CW densities. Here q is the elementary charge, ε_{oD} is the dielectric constant, c is the speed of light in the medium, n is the refractive index, m^* is the effective mass of the carrier (electron or hole) and μ is the mobility. This allows the PCR signal to be expressed in the form

$$
P(\omega) \approx F(\lambda_1, \lambda_2) \int_0^L \Delta N(z, \omega) dz \qquad (4)
$$

with

$$
F(\lambda_1, \lambda_2) = \int_{\lambda_2}^{\lambda_1} [1 - R_1(\lambda)](1 + R_b(\lambda)
$$

$$
\times [1 + R_1(\lambda)])\eta_R W_{eR}(\lambda) C(\lambda) d\lambda \qquad (5)
$$

The PCR signal is the integration of Eq. (4) over the image of the detector on the sample and thus is directly proportional to the depth integral of the carrier density in the sample. Consequently, the relative lateral concentration of any defects that affect the carrier density, either by enhancing recombination or altering diffusion coefficients, can be determined by scanning the surface of the wafer with the PCR probe. In addition, frequency scan techniques can be used with the appropriate carrier diffusion model to

obtain quantitative values for the four transport parameters [6]. This quantitative technique can be combined with the lateral maps to provide quantitative imaging of the semiconductor sample.

3. PCR Imaging NDT of electronic defects in Si wafers

3.1. Instrumentation and signal characteristics

The experimental implementation of laser infrared photo-carrier radiometry is similar to the typical PTR set-up for semiconductors [1,6], with the crucial difference being that the spectral window of the IR detector and optical filter, and the modulation frequency response of the preamplifier stage, must be tailored through spectral bandwidth matching to a combination of carrier recombination emissions and effective spectral filtering of the Planck-mediated thermal infrared emission band. Conventional PTR utilizes photoconductive liquid-nitrogen-cooled HgCdTe (MCT) detectors with spectral bandwidth in the 2–12 μm range. This includes the thermal infrared range, 7–12 μm, and only part of the electronic emission spectrum at shorter wavelengths. From experiments with several IR detectors and bandpass optical filters we concluded that emissive infrared radiation from electronic CW recombination in Si is centered mainly in the spectral region below 3 μm. Among near-IR photodetectors, the combination of variable-gain InGaAs detectors with integrated amplifiers, a near-infrared cut-on filter and a spectral response in the <1800-nm range, was found to be most suitable, exhibiting 100% efficient filtering of the thermal infrared emission spectrum from Si as well as maximum signal-to-noise ratio over InGaAs detectors with separate amplifiers and InAs detectors. The IR detector was a switchable-gain InGaAs element (ThorLabs model PDA400), 1-mm in diameter, with spectral response in the 800–1750 nm range, peak response at 1550 nm and frequency bandwidth from dc to 10 MHz. The preamplifier was incorporated into the detector housing, a design which delivered optimal signal-to-noise ratio expressed as a NEP figure of $2.9 - 8.2 \times 10^{-12} \, W/\sqrt{Hz}$. The detector was out-fitted with a specialty long-pass optical filter from Spectro-gon featuring steep cut-on (5% at 1010 nm, 78% at 1060 nm), and transmission range 1042–2198 nm. The cut-on quality of the filter is crucial in PCR as it must block any synchronous pump radiation leakage from reaching the highly sensitive detector. Short-wavelength filtering of optical density 5 or 6 is usually required. The incident Ar-ion laser beam size was 1.06 mm and the power was 20–24 mW. The detector was proven extremely effective in cutting off all thermal infrared radiation: Preliminary measurements using non-electronic materials (metals, thin foils and rubber) showed no responses whatsoever. Comparison with conventional PTR results was made by replacing the InGaAs detector with a Judson Technologies liquid-nitrogen-cooled
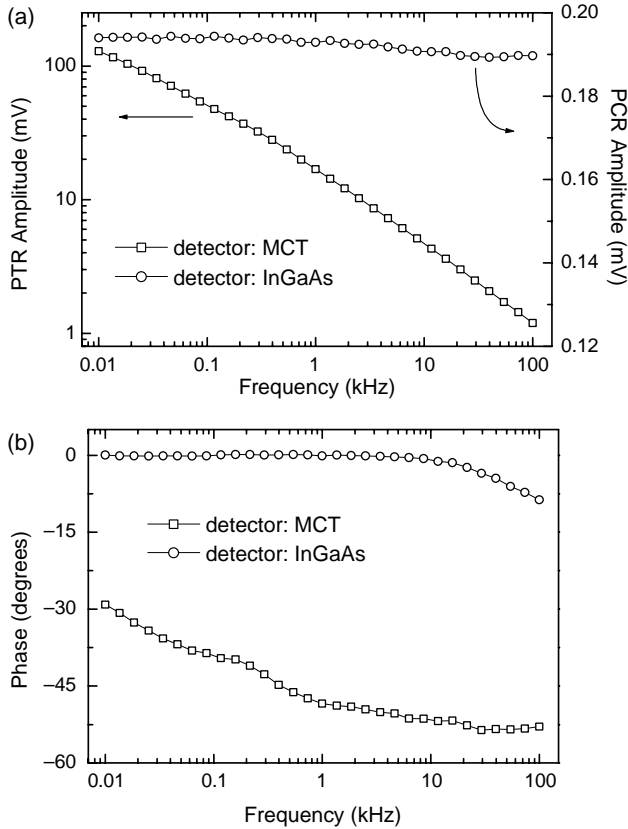
Fig. 2. Comparison of normalized PTR (MCT detector) and PCR (InGaAs detector) signals from an AlGaAs quantum well array on a GaAs wafer. Incident laser power: 25 mW.

Fig. 3. Line scans over a p-Si wafer region with back-surface mechanical damage. (a) PCR amplitude and (b) PCR phase. The wafer is resting on a mirror support. Laser power: 24 mW.

Model J15D12 MCT detector covering the 2–12 μm range with peak detectivity 5×10^{10} cm Hz$^{1/2}$ W^{-1}.

Fig. 2 shows two frequency responses from a test AlGaAs quantum well array on GaAs substrate using both the MCT and the InGaAs detectors. The MCT response is characteristic of thermal-wave domination of the PTR signal throughout the entire modulation frequency range of the lock-in amplifier. On the other hand, the PCR signal from the InGaAs detector/preamplifier exhibits very flat amplitude, characteristic of purely carrier-wave response and zero phase lag up to 10 kHz, as expected from the oscillation of free carriers in-phase with the optical flux which excites them (modulated pump laser). The apparent high-frequency phase lag is associated with electronic processes in the sample. The PTR signals were normalized for the instrumental transfer function with the thermal-wave response from a Zr alloy reference, whereas the PCR signals were normalized with the response of the InGaAs detector to a small fraction of the exciting modulated laser source radiation at 514 nm. To verify the effect of backing on the PCR signal obtained from a Si wafer, measurements were performed using a mirror and black rubber as backings, in the geometry of Fig. 1. From Eq. (2) and known values of the backing emissivity [12] it is expected that the ratio of PCR signals with mirror and black rubber backings should be approx. $[2 + R_1(\lambda)]/[1 + R_b(\lambda)[1 + R_1(\lambda)]] \approx 1.94$.

The measured ratio from the low-frequency end frequency scans was found to be ~1.8.

3.2. PCR imaging of deep sub-surface electronic defects

Fig. 3 shows line scans with the excitation laser beam scanning the front (polished) surface of a 20 Ωcm p-type Si wafer and the IR detector on the same side. Based on the backing results, for maximum signal strength the sample was resting on a mirror. At all three selected modulation frequencies, the PCR amplitude decreases when the laser beam scans over the defect region, consistent with the expected CW density decrease as the back-surface defect efficiently traps carriers and removes them from further diffusion and potential radiative recombination. The PCR phase scan remains essentially constant at 10 Hz, Fig. 3b, as the diffusion-wave centroid is solely determined by the ac carrier-wave diffusion length [1,3]

$$L_{ac}(\omega) = \sqrt{\frac{D^*\tau}{1 + i\omega\tau}} \qquad (6)$$

where τ is the lifetime and D^* is the ambipolar carrier diffusion coefficient. This particular wafer was measured to have $\tau \cong 1$ ms and $D^* \cong 12$ cm^2/s, which yields an $|L_{ac}(10$ - Hz$)| \cong 1.1$ mm. Therefore, the CW centroid lies well beyond

the thickness of the wafer (∼630 μm) and no phase shift can be observed. At the intermediate frequency of 1360 Hz, $|L_{ac}| \cong 373$ μm, well within the bulk of the wafer. In this case, a phase lead appears within the defective region. This occurs because the CW spatial distribution across the body of the wafer in the defective region is weighed more heavily toward the front surface on account of the heavy depletion occurring at, and near, the back surface. As a result, the CW centroid is shifted toward the front surface, manifested by a phase lead. Finally, at 100 kHz, $|L_{ac}| \cong 44$ μm. Nevertheless, Fig. 3a shows that there is still PCR amplitude contrast at that frequency, accompanied by a small phase lead, Fig. 3b.

To maximize PCR imaging contrast, differences in amplitudes and phases as a function of frequency were obtained outside and inside the defective region. It is with the help of this type of analysis that the 1360 Hz frequency was chosen as one with the highest contrast in phase (but not in amplitude). Fig. 4 shows images of the back-surface defect obtained through front-surface inspection at the optimum
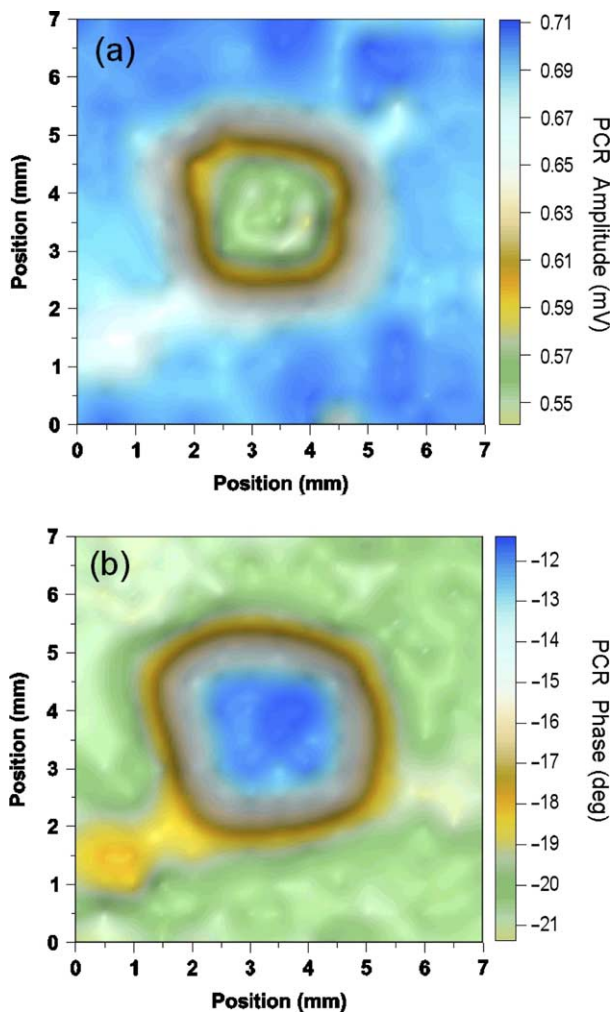
Fig. 4. Scanning imaging of back-surface defect in the p-Si wafer using front-surface inspection. Laser beam radius: 518 μm. Frequency: 1360 Hz. (a) PCR amplitude and (b) PCR phase.
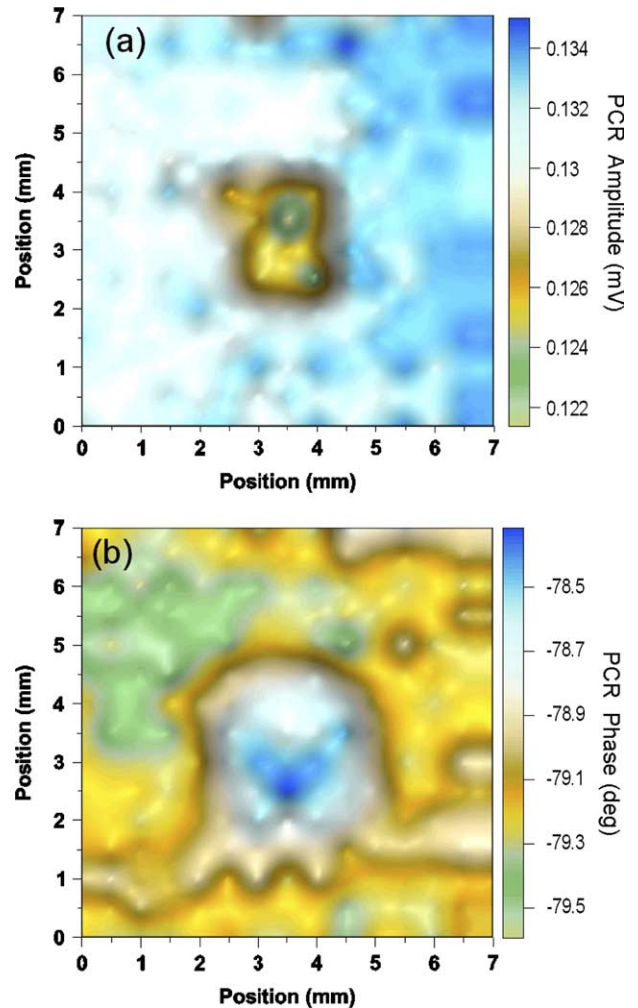
Fig. 5. Scanning imaging of back-surface defect in the p-Si wafer using front-surface inspection. Laser beam radius: 518 μm. Frequency: 100 kHz. (a) PCR amplitude and (b) PCR phase.

contrast frequency of 1360 Hz. Fig. 5 shows the same scan at 100 kHz. At this frequency the PCR image clearly shows the highest spatial resolution of the back-surface defect possible. The PCR phase, Fig. 5b, shows details of the central defect as well as the radially diverging defect structures at the base of the central defect, like a 'zoomed in' version of the 1360 Hz image, Fig. 4b. Both PCR images clearly reveal internal sub-structure of the central defect, which was invisible at 1360 Hz. In a manner reminiscent of conventional propagating wavefields, image resolution increases with decreasing carrier wavelength, $|L_{ac}|$.

Under front-surface inspection and precise depth profilometric control by virtue of the PCR modulation-frequency-adjustable carrier-wave diffusion length, Eq. (6), Figs. 4 and 5 show for the first time that with today's high-quality, long-lifetime industrial Si wafers, one can observe full images of sharp carrier-wave density contrast due to underlying defects very deep inside the bulk of a Si wafer. Specifically, high frequency PCR imaging reveals so far

unknown very long-range effects of carrier interactions with deep sub-surface defect structures and the detrimental ability of such structures to decrease the overall free photoexcited-carrier density far away from the defect sites at or near the front surface where device fabrication takes place. This phenomenon may be important toward device fabrication improvement through careful selection of substrate wafers with regard to deep bulk growth and manufacturing defects which were heretofore not associated with device performance. Further PCR imaging experiments with shorter lifetime Si wafers have shown that it may be beneficial to use lower quality starting substrates in order to avoid the full effects of deep sub-surface defects on the electronic quality of the upper (device-level) surface.

4. Quantitative PCR measurements of electronic transport properties

The PCR image contrast of Figs. 4 and 5 can, in principle, be quantified by use of the CW term in Eq. (4), appropriately modified to accommodate the defective region

$$\Delta P(\omega) \approx F_2(\lambda_1, \lambda_2) \left[\int_0^L \Delta N(z,\omega)\mathrm{d}z - \int_0^L \Delta N_{\mathrm{d}}(z,\omega)\mathrm{d}z \right] \quad (7)$$

where $\Delta P(\omega)$ is the difference in signal between the intact and defective regions. This is a complex quantity, so it can be separated out into amplitude and phase components. The apparent simplicity of this expression is due to the fact that the sub-surface defects considered here are on the back surface of the wafer and their presence mostly impacts the value of the back-surface recombination velocity S_2 [3], while the bulk transport parameters and the terms comprising the prefactor $F(\lambda_1, \lambda_2)$, remain essentially unaltered for a thin damage layer in an otherwise homogeneous semiconductor. If these conditions are not fulfilled, then a more complete (and complicated) expression of the carrier recombination related emissions must be used to quantify PCR contrast due to distributed sub-surface electronic defect structures.

The mild mechanical defect on the back surface of the p-type Si wafer that generated the images of Figs. 4 and 5 proved to be too severe for our sensitive InGaAs photodetector: upon scanning the affected surface the PCR signal vanished within the region of the defect, apparently due to the highly efficient trapping of the photogenerated free carriers by the high density of near-surface electronic defect states. Therefore, a different region of the same wafer was chosen to create a visually undetectable defect by simply touching the back surface of the wafer with paper. Then, PCR frequency scans were performed on both sides of the material, outside and inside the defect region, Fig. 6. The inherent instrumental
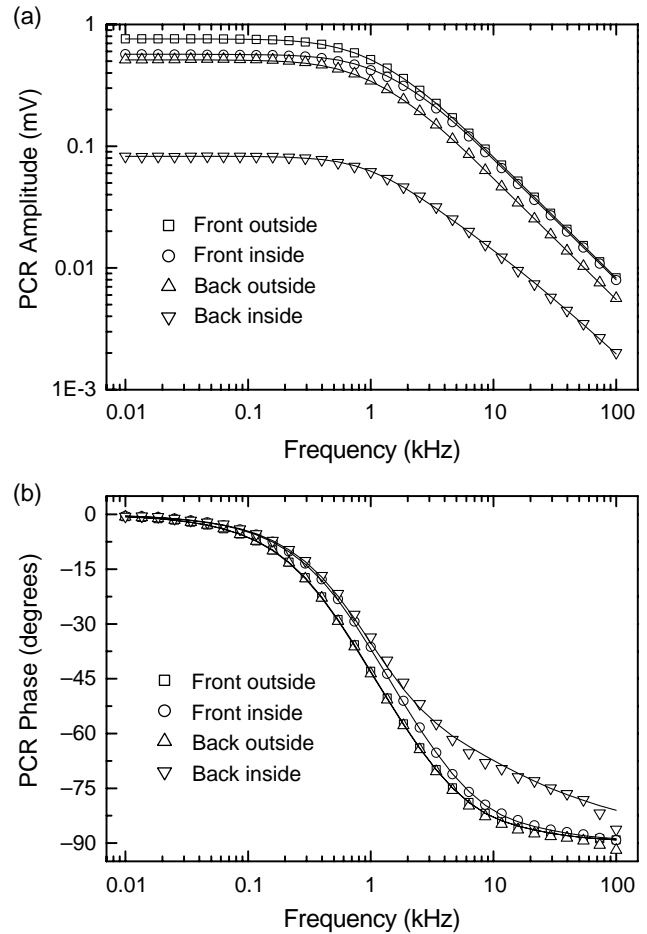
Fig. 6. Front—and back-surface PCR frequency scans inside and outside a defect area of a p-Si wafer on aluminum backing. Detector, InGaAs; beam size, 1.4 mm; Ar-ion laser power, 20 mW. (a) Amplitudes and (b) phases. Best-fit parameters: front intact region: $\tau = 1$ ms; $D^* = 12$ cm²/s, $S_1 = 10$ cm/s, $S_2 = 210$ cm/s. Front inside the defect: $\tau = 1$ ms; $D^* = 14.9$ cm²/s, $S_1 = 25$ cm/s, $S_2 = 300$ cm/s. Back intact region: $\tau = 1$ ms; $D^* = 12$ cm²/s, $S_1 = 10$ cm/s, $S_2 = 200$ cm/s. Back inside the defect: $\tau = 1$ ms; $D^* = 5$ cm²/s, $S_1 = 450$ cm/s, $S_2 = 130$ cm/s.

transfer function was removed by introducing an indirect normalization method based on the fact that in the high frequency regime both HgCdTe and InGaAs detectors monitor the same electronic processes [9]. Therefore, the instrumental normalization of the PCR signal could be performed by mathematically extracting the electronic component of the PTR signal from a good quality wafer and then adjusting the PCR signal to that component. All curves shown here were normalized by the same transfer function obtained by this method. The PCR theoretical model involved carrier-wave IR emissions using diffusion-wave field expressions (Ref. [3], Chap. 9.12), with adjustable electronic transport coefficients [6,13]. The effect of the back-surface defect was modeled as a change in the recombination velocity S_2 (front-surface probing) only. When the wafer was turned over, the definitions of S_1 and S_2 were reversed. Regarding the D^* values, those outside the defect remained constant for both sides of the

wafer, however, the D^* value from the back inside the defect region was relatively low. The high sensitivity of the InGaAs detector to the electronic state of the inspected surface is probably responsible for this discrepancy, as the theoretical phase fit is poor at high frequencies (>1 kHz) within that region, an indication of near-surface depth inhomogeneity of transport properties.

5. Application to quantitative determination of carrier mobility

Carrier mobility (μ) is an important phenomenological parameter for describing the operation of semiconductor devices such as MOSFETs and solar cells. It is one of the basic input parameters for expressing electrical current in devices. In addition, the determination of doping level in wafers requires knowledge of carrier mobility. Several techniques have been used in determining carrier mobilities in semiconductors [14]. However, they all require samples specially prepared or, when this is not the case, they require electrical contacts for signal acquisition. PCR appears to be the first all-optical and non-contacting NDT methodology for determination of carrier mobility. In the experiments the laser beam size at the sample surface was 1.34 mm. Temperature ramps were introduced by a heater/temperature controller. The entire process was controlled by a computer. The heating system was capable of varying and maintaining the sample temperature up to 675 K. One FZ n-type silicon wafer with resistivity $\rho = 10-15 \, \Omega$ cm, $N \sim 8 \times 10^{14}$ cm^{-3}, and a 980-Å thermally grown SiO$_2$ layer was studied. The wafer thickness (l) was 530 μm.

Fig. 7 shows the PCR experimental amplitude and phase frequency responses at different temperatures. The measured temperature range was 300–575 K, given a fixed increment of 25 K. For the sake of clarity, however, only six of the twelve data sets are shown. In the same figure, shown are the results of the best multi-parameter fitting using the theory based on Eq. (4). There is very good agreement between the theory and experimental data for all temperatures. With one frequency scan it is possible to obtain simultaneously the carrier lifetime, diffusion coefficient, and surface recombination velocity. As can be seen, the PCR amplitude increases with temperature. There are two phenomena contributing to this behavior. The first one follows the Shockley–Read–Hall theory [15,16], which assumes that the thermally excited carrier density partially neutralizes existing ionized impurities by increasing the occupation of empty states. Therefore, the photo-injected density of free carriers increases, consequently increasing the carrier-wave recombination emission. This is directly associated with an increase of free carrier lifetime, as shown in Fig. 8. The second contribution accounts for increasing of scattering mechanisms with temperature, which results in a decrease of carrier diffusivity, as shown in Fig. 9. The symbols represent experimental values and
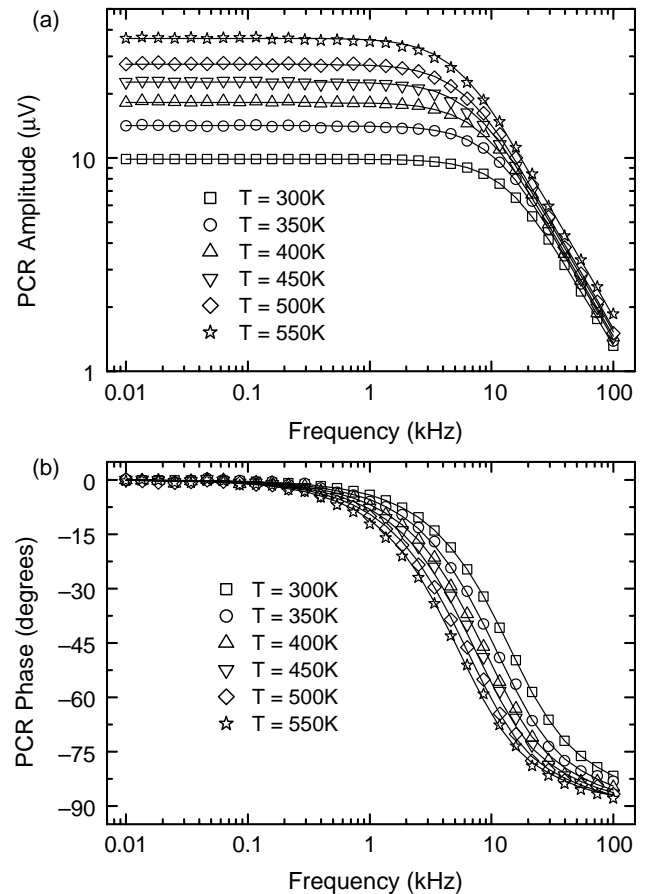
Fig. 7. (a) PCR amplitudes and (b) phase frequency responses at different temperatures. Only six of the 12 data sets are shown. The symbols represent experimental data points, while the lines are the best fitting to data. Laser power, 15 mW; beam size, 1.34 mm.

the line is the result of data fitting using a polynomial function of the form: $D(T) = a \times T^b$. The value obtained for the exponent b ($b = -1.49 \pm 0.01$) is in excellent agreement with that reported in the literature [17], where, using PTR detection, the diffusion coefficient is found to have the
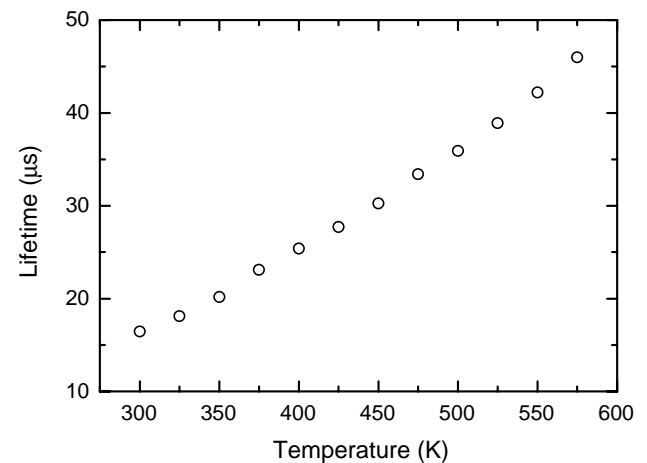
Fig. 8. Lifetime temperature dependence obtained by simultaneously fitting amplitude and phase frequency responses of Fig. 7.
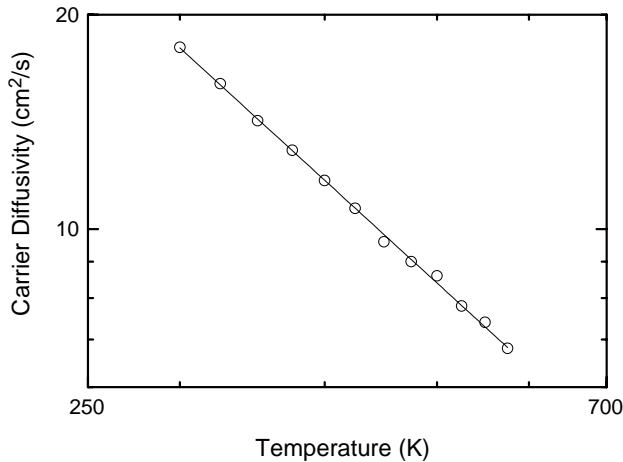
Fig. 9. Temperature dependence of ambipolar diffusion coefficient obtained by simultaneously fitting amplitude and phase frequency responses of Fig. 7. The symbols represent experimental values, while the line is the best fit using the function $D(T) = a \times T^b$, where $a = (8.75 \pm 0.73) \times 10^4$ and $b = -1.49 \pm 0.01$.

following dependence on temperature: $D(T) \sim T^{-1.5}$. Lower diffusion coefficients amount to a higher probability of a carrier to remain within the PCR detection area before the de-excitation processes. A decreasing front surface recombination velocity with increasing temperature was observed: from 166 cm/s at 300 K to values less than 5 cm/s when the temperature approaches 575 K. This result was expected, since recombination velocity is inversely proportional to surface recombination lifetime. The latter is expected to increase as thermally excited carriers increase the occupation probability of both bulk and surface impurity and defect electronic states. The PCR signal was not sensitive to changes in the back surface recombination velocity because the wafer is electronically thick ($L \ll l$) for all values of the carrier-wave diffusion length. The maximum value for L was about 177 μm at 10 Hz, much smaller than the wafer thickness (530 μm). The carrier diffusion coefficient is a key parameter for mobility determination. It is assumed that carrier transport in wafers under intensity-modulated optical excitation occurs predominantly by diffusion. In the relatively low injection level regime, the carrier transport can be described by Boltzmann statistics and hence the mobility is related to the carrier diffusion coefficient by the Einstein relation $D = (kT/q) \mu$, where k is the Boltzmann constant, T is the absolute temperature and q is the elementary charge. Therefore, if the diffusion coefficient is known at different temperatures, the temperature dependence of carrier conductivity mobility can be determined. Fig. 10 shows the temperature dependence of the experimental carrier mobility (symbols) along with the best fit (full line) using the same polynomial function as used for carrier diffusivity. The values of mobility were appropriately normalized by their corresponding thermal voltages (kT/q). The temperature depen-
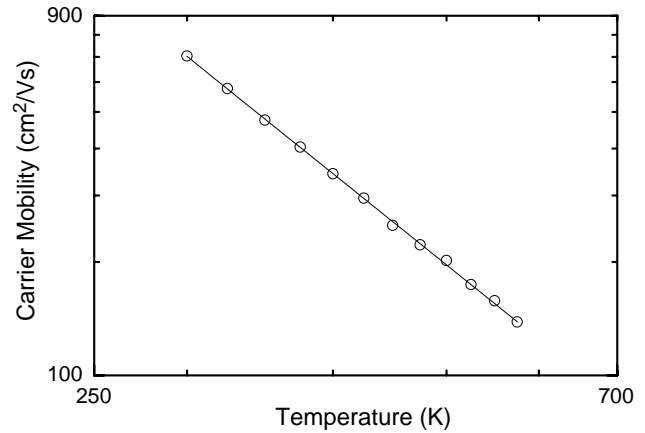
Fig. 10. Temperature dependence of mobility. The symbols represent experimental values, while the line is the best fit using the function $\mu(T) = a \times T^b$, where $a = (1.06 \pm 0.07) \times 10^9$ and $b = -2.49 \pm 0.01$.

dence of carrier mobility obtained could be expressed as:

$$\mu(T) = (1.06 \pm 0.07) \times 10^9 \times T^{-2.49 \pm 0.01} \text{ cm}^2/\text{Vs} \qquad (8)$$

A similar result ($\mu_n(T) = (2.1 \pm 0.2) \times 10^9 \times T^{-2.5 \pm 0.1}$ cm²/Vs and $\mu_n(T) = (2.3 \pm 0.1) \times 10^9 \times T^{-2.7 \pm 0.1}$ cm²/Vs) was reported previously [18,19] using the Hall effect for determining the mobility of electrons and holes in Si, respectively. In a different study [20], a semi-empirical model was proposed and applied to several sets of data from the literature, and values in between 2.2 and 2.4 were found for the constant b, the temperature power in Si samples.

The mobilities of carriers in non-polar semiconductors are determined by interactions with the acoustical vibrations (phonons) of the lattice as well as by scattering by ionized impurities or other defects. The temperature dependence of mobility predicted by the deformation potential theory [21] is $\sim T^{-3/2}$. However, as mentioned above, experimentally measured dependencies differ from this value of ($-3/2$). Reasons for this discrepancy include: (a) contributions from other scattering mechanisms may be present (for example, above 100 K the contribution of optical phonon scattering becomes considerable, which lowers the value of the mobility); and (b) the non-parabolicity, distortion of equi-energy surfaces and the effect of split-off sub-band holes [22].

6. Conclusions

Laser infrared photo-carrier radiometry (PCR) has been introduced. The emerging technology is a novel all-optical photonic method based on carrier diffusion-wave diagnostics. Based on the theoretical foundations and the first few experimental case studies using industrial-quality Si wafers, there are excellent prospects for PCR as an in-situ NDT quality control technology in semiconductor processing and manufacturing. Its localized high-resolution monitoring nature surpasses the currently available techniques for

non-destructive, non-contact monitoring and imaging of deep electronic defects in Si wafers, for measuring free-carrier transport properties, and for measuring carrier mobilities without the need for auxiliary electric circuit fabrication and electrode application. PCR may become a valuable NDT technology as it can monitor local values of carrier mobilities and other transport properties at several intermediate stages of device fabrication. A noteworthy feature of high frequency PCR imaging is that it has revealed for the first time a very long-range effect of carrier interactions with deep sub-surface defect structures and the detrimental ability of such structures to decrease the overall free photoexcited-carrier density in locations far away from the defect sites at or near the front surface where device fabrication takes place. Therefore, PCR may become an important tool toward device fabrication improvement through careful selection of substrate wafers with regard to deep bulk growth and manufacturing defects which were heretofore not associated with device performance.

Acknowledgements

References

[1] Mandelis A. Solid-State Electron. Laser Infrared Photothermal Radiometry of Semiconductors: Principles and Applications to Solid-State Electronics 1998;42(1):1–15.

[2] Christofides C, Nestoros M, Othonos A. In: Mandelis A, Hess, P, editors. Semiconductors and Electronic Materials (Progress in Photoacoustic and Photothermal Phenomena; vol. IV). Bellingham, WA: SPIE, 2000 chapter 4.

[3] Mandelis A. Diffusion-wave fields: mathematical methods and green functions. New York: Springer; 2001: p. 9.

[4] Wagner RE, Mandelis A. Nonlinear photothermal modulated optical reflectance and photocurrent phenomena in crystalline semiconductors: II Experimental. Semicond. Sci. Technol 1996;11:300–7.

[5] Salnick A, Mandelis A, Ruda H, Jean C. Relative Sensitivity of photomodulated reflectance and photothermal infrared radiometry to thermal and carrier plasma waves in semiconductors. J. Appl. Phys. 1997;82(4):1853–9.

[6] Rodriguez ME, Mandelis A, Pan G, Nicolaides L, Garcia JH, Riopel Y. Computational aspects of laser radiometric multiparameter fit for carrier transport property measurements in Si wafers. J. Electrochem. Soc. 2000;147(2):687–98.

[7] Rosencwaig A. In: Mandelis A, editor. Photoacoustic and thermal-wave phenomena in semiconductors. New York: North-Holland, 1987 chapter 5.

[8] van Roosbroeck W, Shockley W. Photon-radiative recombination of electrons and holes in germanium. Phys. Rev. 1954;94(6):1558–60.

[9] Mandelis A, Batista J, Shaughnessy D. Infrared photo-carrier radiometry of semiconductors: Physical principles, quantitative depth profilometry and scanning imaging of deep sub-surface electronic defects. Phys. Rev. B 2003;67: 205208 1–18.

[10] Kirchhoff G. Abhandlungen über Emission und Absorption. M. Planck, editor. Leipsig: Verlag von Wilhelm Engelmann; 1898. p. 11–36.

[11] Smith RA. Semiconductors. 2nd ed; 1978. p. 118–9.

[12] Kreit F, Black WZ. Basic heat transfer. New York: Harper and Row, 1980.

[13] Ikari T, Salnick A, Mandelis A. Theoretical and experimental aspects of three-dimensional infrared Photothermal Radiometry of Semiconductors. J. Appl. Phys. 1999;85(10):7392–7.

[14] Schroder DK. Semiconductor Material and Device Characterization, 2nd ed. New York: Wiley-Interscience, 1998.

[15] Shockley W, Read WT. Statistics of the Recombinations of Holes and Electrons. Phys. Rev. 1952;87(5):835–42.

[16] Hall RN. Electron-Hole Recombination in Germanium. Phys. Rev. 1952;87(2):387.

[17] Salnick A, Jean C, Mandelis A. Noncontacting Photothermal Radiometry of SiO2/Si MOS Capacitor Structures. Solid-State Electron. 1997;41(4):591–7.

[18] Mette H, Gartner WM, Loscoe C. Nernst and Ettingshausen Effects in Silicon between 300°K and 800°K. Phys. Rev. 1960;117(6):1491–3.

[19] Ludwig GW, Watter RL. Drift and Conductivity Mobility in Silicon. Phys. Rev. 1956;101(6):1699–701.

[20] Mnatsakanov TT, Pomortseva LI, Yurkov SN. Semiconductors 2001; 35:394.

[21] Bardeen J, Shockley W. Deformation Potentials and Mobilities in Non-Polar Crystals. Phys. Rev. 1950;80(1):72–80.

[22] Takeda K, Sakudi K, Sakata M. Temperature dependence of mobility and Hall coefficient factor for holes of highly pure silicon. J. Phys. C: Solid State 1982;15(4):767–76.